IOPscience iopscience.iop.org

Home Search Collections Journals About Contact us My IOPscience

A molecular dynamics investigation of longitudinal collective modes in metal-salt solutions

This article has been downloaded from IOPscience. Please scroll down to see the full text article.

1993 J. Phys.: Condens. Matter 5 5701

(http://iopscience.iop.org/0953-8984/5/32/002)

View the table of contents for this issue, or go to the journal homepage for more

Download details:
IP Address: 171.66.16.96
The article was downloaded on 11/05/2010 at 01:35

Please note that terms and conditions apply.

J. Phys.: Condens. Matter 5 (1993) 5701–5722. Printed in the UK

A molecular dynamics investigation of longitudinal collective modes in metal–salt solutions

Alberto Meroni† and Jean Pierre Hansen

Laboratoire de Physique‡ de l'Ecole Normale Supérieure de Lyon, 46 Allée d'Italie, 69364 Lyon Cédex 07, France

Received 9 March 1993, in final form 11 June 1993

Abstract. Results are reported of extensive molecular dynamics (MD) simulations of a simple model of the prototype metal–salt solution $K_x(KCl)_{1-x}$. The Coulomb interactions between ions are assumed to be screened by the degenerate valence electrons, within the Thomas–Fermi approximation. The main emphasis is on the concentration (x) dependence of the density and charge fluctuation spectra. The MD data for these spectra are analysed in terms of the extended mode concept, by fitting the data to superpositions of Lorentzians, with wavenumber-dependent coefficients. This analysis clearly shows the emergence, in addition to an extended acoustic (sound) mode, of a high-frequency optic mode at intermediate and low metal concentrations x. This mode may be considered as a remnant of the well known propagating charge fluctuation (or plasmon) mode in molten salts; at finite x the optic mode is strongly affected by electron screening. The subtle interplay between acoustic and optic modes is in qualitative agreement with the predictions of a recent generalized hydrodynamics analysis.

1. Introduction

There are two main classes of conducting liquid: liquid metals or alloys, which exhibit large electrical conductivities associated with the highly mobile valence electrons, and ionic liquids including molten salts and ionic solutions with much lower conductivities, which originate in the mutual diffusion of anions and cations. A very interesting combination of metallic and ionic behaviour may be found in molten mixtures of metals and salts that share the same cation. The simplest and most widely studied among these are solutions of alkali metals in their halides, of the form $M_x(MX)_{1-x}$, where M denotes the metal, X the halogen and x is the mole fraction of metal. As x is varied from zero to one, the melt changes continuously from a pure ionic liquid, the alkali halide MX, to a pure liquid metal. Upon decreasing x, the initially nearly free valence electrons undergo a continuous metal–non-metal transition towards highly localized states, as signalled by a rapid drop of the electrical conductivity; in the pure-salt limit no valence electrons are left, and the conductivity is purely ionic in nature.

The gradual change in electronic structure gives rise to a number of remarkable thermodynamic and structural properties of $M_x(MX)_{1-x}$ melts. The melting temperature drops by more than a factor of two between the salt and metal limits. Some of the melts, like $Rb_x(RbBr)_{1-x}$, exhibit a miscibility gap at intermediate concentrations [1], and strong concentration fluctuations are signalled by intense small-angle scattering in

† Present address: Dipartimento di Fisica, Universitá degli Studi di Milano, Italy.

‡ Unité de Recherche Associée au Centre National de la Recherche Scientifique (URA 1325).

0953-8984/93/325701+22$07.50 © 1993 IOP Publishing Ltd

neutron diffraction experiments [2], even in solutions like $K_x(KCl)_{1-x}$, which mix at all concentrations. The latter solution is found to expand at constant temperature, as electrons progressively replace the anions, from about $50\,cm^3\,mol^{-1}$ for pure KCl, to about $60\,cm^3\,mol^{-1}$ for pure K, at $T \simeq 1000\,K$. The change in molar volume with x deviates strongly from linearity, giving rise to an unusually large excess molar volume, which moreover changes from negative to positive values as x increases [3]. The ionic pair structure, as measured by neutron scattering experiments [2], changes dramatically with concentration, and crosses over from metallic like to ionic like at unexpectedly high values of x ($x \simeq 0.85$), indicating the strong influence of charge ordering.

Many of these features are reproduced, at least qualitatively, by simple models of metal–salt solutions, where the valence electrons are replaced by a neutralizing background, which is treated either as rigid [4,5] or polarizable [6]. While this oversimplification of the electronic structure may be reasonable on the metal-rich side ($x \simeq 1$), where the relatively weak ion–electron coupling is well described by second-order perturbation theory [7], it does lead to some significant discrepancies with experiment at intermediate concentrations, in particular as regards the small-angle scattering, or the sign of the excess molar volume. Despite their shortcomings, the above-mentioned models have been extended to investigate dynamical collective modes in simple metal–salt solutions, for which much fewer experimental data are available, but which are the object of current inelastic neutron scattering experiments [8]. The long-wavelength collective modes of the rigid electron background model have been analysed within linearized hydrodynamics [9]; the main prediction of this analysis is the overdamping of the sound mode, which ceases to propagate below a concentration-dependent critical wavenumber on the salt-rich side. However, strictly speaking, this prediction applies only to the rather unphysical model for the electronic structure; electron polarization and screening are expected to induce qualitative changes in the ionic density and charge fluctuation spectra [9–11]. Moreover, the hydrodynamic analysis only applies to low frequencies, and the frequency dependence of the ionic conductivity must be allowed for in order to investigate the high-frequency optic mode [9, 12]. Electron polarization is approximately accounted for in a model where ions interact via effective screened Coulomb potentials. In [13] the memory function formalism was used to examine the longitudinal collective modes of the screened Coulomb model for $K_x(KCl)_{1-x}$. This analysis pointed to an interesting concentration dependence of the dispersion curves and to a subtle interplay between acoustic and optic branches of the longitudinal excitation spectrum at intermediate wavenumbers, accessible to inelastic neutron scattering experiments.

The main objective of the present work is to check and extend the predictions of [13] by 'exact' molecular dynamic (MD) simulations of the same model. The calculated density and charge fluctuation spectra are analysed, assuming the validity of the extended hydrodynamic mode concept of De Schepper and Cohen [14], which has been successfully used in recent analyses of inelastic neutron scattering spectra of simple liquids [15]. In addition to the data on the dispersion and damping of the collective modes, the present MD simulations also yield information on the concentration dependence of the pair structure, and on the self-diffusion of the anions and cations.

2. The screened Coulomb model

The $M_x(MX)_{1-x}$ melt contains N_1 cations of charge $+e$ and mass m_1, N_2 anions of charge $-e$ and mass m_2, and $N_0 = N_1 - N_2$ valence electrons ensuring overall electrical neutrality.

Let $N = N_1 + N_2$ be the total number of ions; the number concentrations are $x_\alpha = N_\alpha/N$ ($\alpha = 1,2$), while the molar concentration of metal is $x = (x_1 - x_2)/x_1$.

If V denotes the total volume occupied by the melt, the total ionic and electronic number densities are $n = N/V$ and $n_0 = nx/(2-x)$. A convenient length scale is the ion sphere radius $a = (3/4\pi n)^{1/3}$. The ions are assumed to interact via the following set of model pair potentials:

$$v_{\alpha\beta}(r) = (1 - \delta_{\alpha\beta})B \exp(-Ar) + \frac{z_\alpha z_\beta e^2}{r} e^{-r/\lambda} \tag{2.1}$$

where $1 \leqslant \alpha, \beta \leqslant 2$ are species indices, $\delta_{\alpha\beta}$ is the Kronecker symbol, and $z_\alpha = \pm 1$ is the valence of ion species α.

The first term on the RHS of (2.1) describes the short-range Born–Mayer repulsion between unlike ions; the parameters A and B are chosen to be identical to those of the Tosi–Fumi potential for the corresponding pure molten salt ($x = 0$) [16] ($A = 2.967\,\text{Å}^{-1}$, $B = 2.86 \times 10^{-9}$ erg). The second term is the screened Coulomb potential between ions. The screening length λ is determined by the Fermi gas of valence electrons. In the linear response regime, the exact long-wavelength ($k \to 0$) limit of the dielectric function $\epsilon_0(k)$ yields the following expression for λ [17]:

$$\kappa^2 \equiv \lambda^{-2} = k_{\text{TF}}^2 \frac{\chi_{\text{TO}}}{\chi_{\text{TO}}^{\text{id}}} \tag{2.2}$$

where k_{TF} is the Thomas–Fermi wavenumber, χ_{TO} and $\chi_{\text{TO}}^{\text{id}}$ are the isothermal compressibilities of the interacting and ideal electron gases respectively. The familiar Thomas–Fermi result is recovered if electron correlations are neglected, i.e. if $\chi_{\text{TO}} = \chi_{\text{TO}}^{\text{id}}$. k_{TF} is density and temperature dependent, but except at very low metal concentrations ($x \to 0$) the Fermi temperature T_{F} of the valence electrons greatly exceeds the thermodynamic temperature T, so that the temperature dependence may be safely neglected, i.e. k_{TF} may be taken equal to its zero-temperature value (degenerate Fermi gas):

$$k_{\text{TF}} = \frac{2}{a_{\text{B}}^{1/2}} \left(\frac{3}{\pi}\right)^{1/6} n_0^{1/6} \tag{2.3}$$

where $a_{\text{B}} = \hbar^2/m_0 e^2$ is the Bohr radius. The screening length $\lambda_{\text{TF}} = k_{\text{TF}}^{-1}$ thus slowly increases as the metal concentration is lowered, and diverges in the pure-salt limit $x = 0$, where the ions interact via the bare (unscreened) Coulomb potential. The potential model (2.1) reduces in that limit to the rigid-ion Tosi–Fumi potential, without the attractive van der Waals dispersion terms that are expected to contribute significantly to the thermodynamic properties, in particular to the pressure, but should much less affect the pair structure. This point was confirmed by an explicit comparison of the partial structure factors $S_{\alpha\beta}(k)$ calculated with and without the dispersion terms in [13].

The linear screening description is known to be reasonably accurate in the pure-metal limit [7], but the Thomas–Fermi form of the electron dielectric function $\epsilon_0(k)$ is too crude an approximation to yield a realistic effective pair potential between cations. In fact, it was shown in [13] that the Thomas–Fermi approximation overestimates the screening power of the degenerate electron gas, because of the improper treatment of the Pauli principle. It was further shown that a proper rescaling of the Thomas–Fermi screening length in the pair potential (2.1) leads to a significant improvement in the agreement between the theoretical

and experimental structure factors for liquid K around $T \simeq 1000\,\mathrm{K}$. Thus the screening length was chosen to be

$$\lambda(x) = \zeta \lambda_{\mathrm{TF}}(x) \tag{2.4}$$

where the best agreement between theory and experiment is achieved for $\zeta \simeq 1.6$ in the pure metal ($x = 1$). The same value of the scaling factor ζ was subsequently kept for all other concentrations; hence, the concentration dependence of the screening length is entirely contained in the Thomas–Fermi behaviour (2.3).

These prescriptions uniquely determine the state-dependent pair potentials at all concentrations; this model is not meant to provide a realistic description of the effective interactions between ions, but rather represents the simplest interpolation between the pure-metal and pure-salt states, for which the model (2.1) potential has been shown to yield a satisfactory description [13]. The model is expected to be reasonable for $x = 0$ and on the metal-rich side, but should be at its worst for low but finite metal concentrations, where the valence electrons are known to be highly localized in f-centre-like states [18, 19], which of course cannot be described by the linearly polarized electron background picture.

The data presented in the following sections were obtained from microcanonical (constant-energy) MD simulations of samples of $N = 216$ ions in a cubic cell, with periodic boundary conditions. The nearest-image truncation was applied at all concentrations except $x = 0$ (pure salt), where the unscreened Coulomb interactions were treated by Ewald summation of all periodic images of the ions. The simulations were carried out for potential parameters and ionic masses appropriate for $K_x(KCl)_{1-x}$, and for molar concentrations $x = 0.0$, 0.1, 0.2, 0.3, 0.4, 0.6, 0.8, 0.9 and 1. Note that the masses of K and Cl ions are nearly equal ($m_1 = 39.098$ and $m_2 = 35.453$ atomic mass units); the slightly different physical masses were adopted here, whereas a symmetric model with equal masses was used in [13]. Molar volumes were taken at their experimental values [3], rather than linearly interpolated between the pure-phase ($x = 0$ and 1) values, as in [13]. These two minor differences between the memory function analysis of [13] and the present MD data are not expected to induce important changes in the static and dynamical correlation functions of the model. The coupled equations of motion of the N ions were numerically integrated using the Verlet algorithm, with a timestep (different for each simulation) small enough to ensure a conservation of total energy to better than 1/10 000. The timesteps are reported in table 1, and for each thermodynamic state 3×10^4 steps were taken after initial equilibration (2×10^4 timesteps); the resulting trajectories in phase space extended over several tens of picoseconds, and statistical averages were taken along these trajectories. The relevant thermodynamic parameters for each of the runs are summarized in table 1.

3. Concentration dependence of the static structure

The static structure of a metal–salt solution is conveniently characterized by the three partial pair distribution functions $g_{\alpha\beta}(r)$. In the pure-metal ($x = 1$) limit, only the cation–cation distribution function $g_{11}(r)$ survives, whereas in the pure-salt ($x = 0$) limit, $g_{11}(r) \equiv g_{22}(r)$ as a consequence of the charge conjugation symmetry of the pair potential model (2.1).

The concentration dependence of the pair structure is summarized in figure 1, where the three $g_{\alpha\beta}(r)$ are shown for eight concentrations. As expected, the pure-salt data exhibit pronounced charge ordering, characterized by perfect phase opposition of the oscillations in $g_{12}(r)$ and $g_{11}(r) \equiv g_{22}(r)$.

Table 1. Characteristics of the metal–salt solutions simulated by MD. x is the metal concentration, V_m the molar volume, n the ionic number density, T is the mean temperature, λ the renormalized screening length, D_K and D_{Cl} the self-diffusion coefficients, c_s the sound velocity and Δt the timestep used in the simulations.

x	V_m ($cm^3\,mol^{-1}$)	n 10^2 (ions $Å^{-3}$)	T (K)	λ (Å)	D_K 10^5 ($cm^2\,s^{-1}$)	D_{Cl} 10^5 ($cm^2\,s^{-1}$)	c_s 10^5 ($cm\,s^{-1}$)	Δt (s)
0.0	49.29	2.41	1121	$+\infty$	6.5	5.9	2.10	2.69×10^{-15}
0.1	50.72	2.24	1112	1.787	13.4	12.2	2.10	2.79×10^{-15}
0.2	52.44	2.07	1123	1.614	18.1	14.6	1.86	2.91×10^{-15}
0.3	54.50	1.88	1102	1.519	19.9	18.5	1.47	3.06×10^{-15}
0.4	56.00	1.72	1135	1.454	28.2	27.9	1.41	3.18×10^{-15}
0.6	57.14	1.48	1141	1.365	37.1	35.7	1.58	3.45×10^{-15}
0.8	59.00	1.02	1142	1.307	55.2	39.1	1.88	3.78×10^{-15}
0.9	60.00	1.11	1169	1.285	61.4	38.0	1.93	9.33×10^{-14}
1.0	61.00	0.99	973	1.266	66.0	—	1.95	4.20×10^{-15}

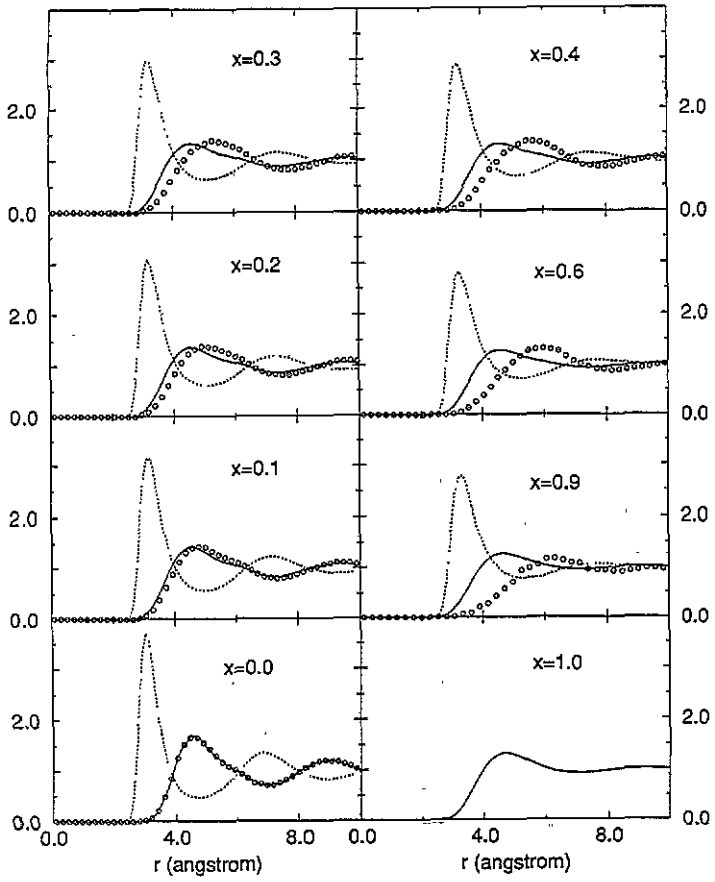

Figure 1. MD-generated partial pair distribution functions $g_{KK}(r)$ (full curves), $g_{KCl}(r)$ (dotted curves) and $g_{ClCl}(r)$ (circles) for $K_x(KCl)_{1-x}$ solutions at concentrations $x =$ 0, 0.1, 0.2, 0.3, 0.4, 0.6, 0.9 and 1; the other thermodynamic parameters are specified in table 1.

As x increases, a splitting of anion–anion and cation–cation correlations is observed, the first peak in $g_{11}(r)$ moving to shorter distances, while that of $g_{22}(r)$ shifts to larger r, but a clear remnant of charge ordering is observed, even up to $x \simeq 0.9$. This behaviour agrees, at least qualitatively, with the predictions of earlier models [5] and of experiment [2], and underlines the predominance of the charge alternation pattern, even when the bare Coulomb interactions (which apply at $x = 0$) are replaced by screened Coulomb interactions, due to valence electron polarization.

The three partial structure factors $S_{\alpha\beta}(k)$ were calculated by direct Fourier transformation of the $g_{\alpha\beta}(r)$. Since no attempt was made to extrapolate the latter to distances r larger than the cutoff imposed by the simulation, finite-size (truncation) effects show up for wavenumbers $k < 2\pi/L$. In figures 2(*a*)–(*d*) a comparison is made between our MD results and the neutron diffraction data of Jal and co-workers [2]. The agreement is seen to be good for $x = 0$ (pure salt) and reasonable (bearing in mind the crudeness of the model) for $x = 1$ (pure metal), as already noted in [13]. The agreement is much less satisfactory at intermediate concentrations ($x = 0.3$ and 0.8), where the MD results do not reproduce the strong small-angle scattering revealed by neutron diffraction data; the sharp rise (or drop) of the experimental partial structure factors at small wavenumbers is symptomatic of strong concentration fluctuations, which are suppressed by the small size of the simulated sample. The screened Coulomb model is also found to underestimate the structure of the experimental data at intermediate wavenumbers, where finite-size effects are expected to be negligible.

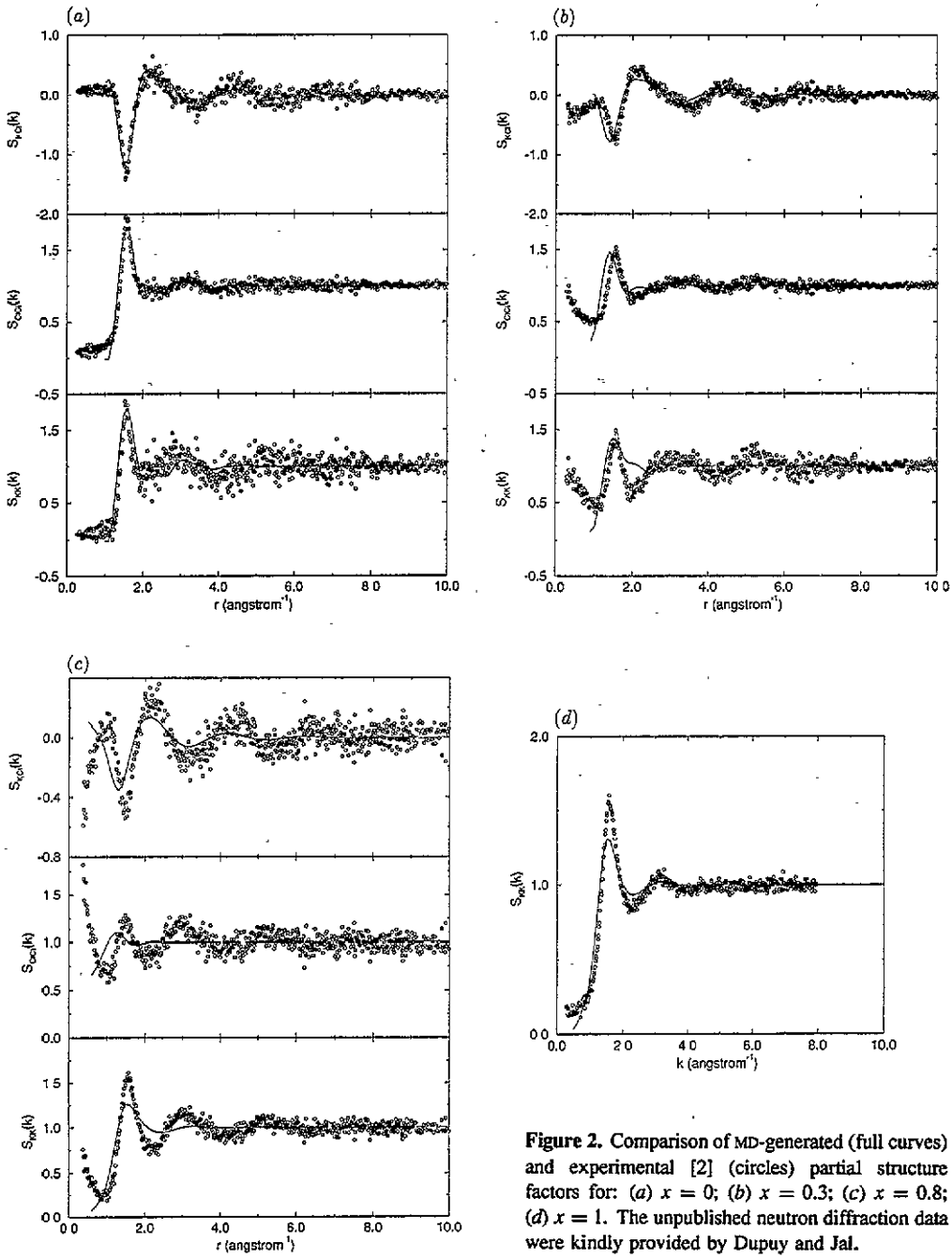

Figure 2. Comparison of MD-generated (full curves) and experimental [2] (circles) partial structure factors for: (*a*) $x = 0$; (*b*) $x = 0.3$; (*c*) $x = 0.8$; (*d*) $x = 1$. The unpublished neutron diffraction data were kindly provided by Dupuy and Jal.

4. Self-diffusion of anions and cations

The self-diffusion constants D_1 and D_2 of the cations and anions were estimated, for each concentration, from the asymptotic behavior of the mean square displacements as functions

of time:

$$D_\alpha = \lim_{t\to\infty} \frac{\langle |r_\alpha(t) - r_\alpha(0)|^2 \rangle}{6t} \tag{4.1}$$

where the statistical average is taken over all ions of species α. Two examples of such Einstein plots are shown in figure 3, and the resulting estimates of D_α are plotted in figure 4. The statistical uncertainty is estimated to be about 5% for the cations, and somewhat larger for the anions at high metal concentrations where few Cl^- ions are left. In the pure salt, the anion and cation diffusion constants agree within statistical uncertainties; within the symmetric potential model (2.1), the two diffusion constants would be strictly identical for equal masses. The values quoted here are close to those obtained with more realistic pair potentials, including attractive van der Waals interactions [20], although the latter data predict D_2 to be slightly larger than D_1. The data summarized in figure 4 indicate a roughly linear increase of D_1 with x, which is not unreasonable in view of the increase of molar volume. Within our model, D_1 increases by an order of magnitude between the pure-salt and pure-metal limits.

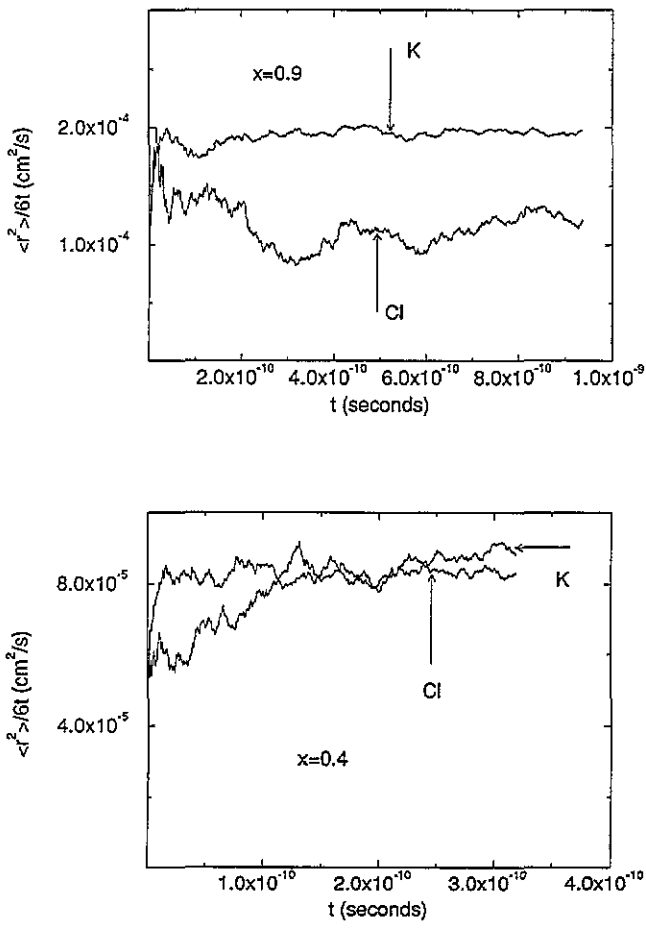

Figure 3. Einstein plot of the mean-square displacement $\langle r^2 \rangle \equiv \langle |r(t) - r(0)|^2 \rangle$ of cations and anions from their initial positions, for $x = 0.4$ (lower curves) and $x = 0.9$ (upper curves).

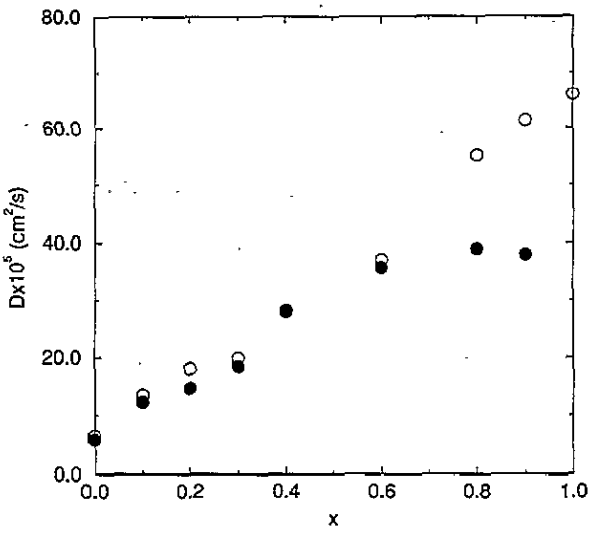

Figure 4. Concentration dependence of the self-diffusion coefficients of cations (open circles) and anions (filled circles); x is the volume fraction of metal.

D_2 appears to lie below D_1 over the whole range of concentrations, but up to $x = 0.6$ the two diffusion constants are fairly close, the difference remaining practically always within the combined error bars. The difference is really significant only at $x = 0.8$ and $x = 0.9$, where the ratio D_1/D_2 is close to two. This can be intuitively understood if we consider that, in this range of concentration, Cl^- ions are embedded in a cloud of K^+ ions and that the screened Coulomb interaction with the latter is attractive, leading in a sense to an effective chlorine mass larger than the physical mass.

5. Extended mode analysis of charge and number density fluctuation spectra

As already stressed in the introduction, the main objective of the present MD simulations is an exploration of the longitudinal collective modes in a range of wavelengths accessible to inelastic neutron scattering experiments. More precisely, we shall focus on the density and charge fluctuation spectra.

The present two-component system admits six collective dynamical variables, which relax slowly in the long-wavelength limit, and are associated with the six macroscopically conserved variables, namely the total numbers of particles of each species, the total momentum and total energy. These dynamical variables are

$$\rho_{k\alpha}(t) = \sum_{i=1}^{N_\alpha} e^{ik\cdot r_{i\alpha}(t)} \qquad \alpha = 1, 2 \tag{5.1a}$$

$$j_{kM}(t) = m_1 j_{k1}(t) + m_2 j_{k2}(t) = \sum_{\alpha=1,2} m_\alpha \sum_{i=1}^{N_\alpha} v_{i\alpha}(t) e^{ik\cdot r_{i\alpha}(t)} \tag{5.1b}$$

$$E_k(t) = \sum_{\alpha=1,2} \sum_{i=1}^{N_\alpha} e^{ik\cdot r_{i\alpha}(t)} \left(\tfrac{1}{2} m_\alpha v_{i\alpha}^2(t) + \frac{1}{2} \sum_{\beta=1,2} \sum_{j\neq i=1}^{N_\beta} v_{\alpha\beta}\left(r_{ij}(t)\right) \right) \tag{5.1c}$$

where $v_{i\alpha}(t)$ denotes the velocity of ion i of species α at time t, and $r_{ij}(t) = |r_{i\alpha}(t) - r_{j\beta}(t)|$ is the interparticle distance of the $(i\alpha; j\beta)$ pair at that time. In the one-component limits,

$x = 1$ and $x = 0$, only five conserved variables are left; in the pure salt ($x = 0$), the five hydrodynamic modes associated with these variables are supplemented by a charge relaxation mode (or longitudinal optic mode), which has a finite lifetime even at $k = 0$ [21].

Since the limited size of the simulation cell precludes the exploration of the long-wavelength (or hydrodynamic) regime, we found it more convenient to focus on two variables that are linear combinations of the partial densities $\rho_{k\alpha}(t)$, namely the number density and the charge density:

$$\rho_{kC}(t) = \rho_{k1}(t) - \rho_{k2}(t) \tag{5.2a}$$

$$\rho_{kN}(t) = \rho_{k1}(t) + \rho_{k2}(t). \tag{5.2b}$$

From these a symmetric two-by-two correlation function matrix may be constructed, with elements

$$F_{ab}(k,t) = \frac{1}{N}\langle \rho_{ka}(t)\rho_{-kb}(0)\rangle \qquad a, b = N \text{ or } C. \tag{5.3}$$

Note that $\rho_{kN}(t)$ is nearly proportional to $\rho_{kM}(t)$ in view of the fact that the mass ratio m_1/m_2 is close to one. The spectra of number and charge density fluctuations are given by the dynamical structure factors:

$$S_{ab}(k,\omega) = \frac{1}{2\pi}\int_{+\infty}^{-\infty} e^{i\omega t} F_{ab}(k,t)\,dt. \tag{5.4}$$

We have systematically computed $F_{NN}(k,t)$ and $F_{CC}(k,t)$ as functions of time for all concentrations x listed in table 1, and for about 20 wavenumbers k, in the range $k_{\min} \leqslant k \leqslant 10k_{\min}$, where $k_{\min} = 2\pi/L$ is the smallest wavenumber compatible with the periodic boundary conditions of the simulation cell; it varies between $0.225\,\text{Å}^{-1}$ (for pure metal) and $0.304\,\text{Å}^{-1}$ (for pure salt). In some instances we also computed the cross correlation function $F_{NC}(k,t)$. In the pure salt, the latter would be identically zero if the masses were strictly equal, due to the charge conjugation symmetry of the potential model (2.1) [22].

In practice, $F_{NN}(k,t)$, $F_{CC}(k,t)$ and $F_{NC}(k,t)$ were computed over a time window $0 \leqslant t \leqslant t_0$, by averaging over time origins along the phase-space trajectory mapped out in the MD simulations; t_0 was typically chosen to be 10% of the total time interval covered by the runs, i.e. $t_0 \simeq 10\,\text{ps}$. This time was always longer than the characteristic relaxation time of the correlation functions or, more precisely, than the time t_C beyond which the signal dropped below the statistical noise level. The computed correlation functions were smoothed by multiplying the signal with a filter function which effectively cut off the noise beyond $t \simeq t_C$, before taking numerical Fourier transforms to calculate the dynamical structure factors $S_{NN}(k,\omega)$, $S_{CC}(k,\omega)$, and $S_{NC}(k,\omega)$.

In the spirit of the extended hydrodynamic mode picture [14, 15], we have analysed $S_{NN}(k,\omega)$ and $S_{CC}(k,\omega)$, by assuming that these spectra may be represented as superpositions of Lorentzians:

$$S(k,\omega) = \frac{A_0(k)}{\omega^2 + \gamma_0^2(k)} + \sum_{\nu=1}^{n}\left(\frac{A_\nu(k)}{[\omega - \omega_\nu(k)]^2 + \gamma_\nu^2(k)} + \frac{A_\nu(k)}{[\omega + \omega_\nu(k)]^2 + \gamma_\nu^2(k)}\right)$$

$$\equiv l_0(k,\omega) + \sum_{\nu=1}^{n}\left[l_\nu(k,\omega) + l_{-\nu}(k,\omega)\right]. \tag{5.5}$$

The form (5.5) automatically satisfies the even parity of $S_{NN}(k,\omega)$ and $S_{CC}(k,\omega)$:

$$S_{aa}(k,-\omega) = S_{aa}(k,\omega).$$

The first Lorentzian, $l_0(k)$, represent the central peak of the spectra, associated with purely diffusive processes, like thermal diffusion or interdiffusion of the two ionic species. The other Lorentzians, centred in conjugate pairs around $\pm\omega_\nu(k)$, correspond to propagating modes ($\omega_\nu \neq 0$). Since the spectra may *a priori* exhibit resonances associated with sound modes and optic modes, we have considered representations of the $S_{aa}(k,\omega)$ involving either one ($n = 1$) or two ($n = 2$) conjugate pairs. The $3n+2$ coefficients $A_0(k)$, $\gamma_0(k)$, $A_\nu(k)$, $\omega_\nu(k)$ and $\gamma_\nu(k)$ were determined, for each k, by least-squares fitting of the representations (5.5) to the MD data for $S_{NN}(k,\omega)$ and $S_{CC}(k,\omega)$.

The practical implementation amounted to minimizing the following mean square deviation:

$$\chi^2_{aa} = \frac{(3n+2)}{p}\sum_{i=0}^{p}\left(S_{aa}(k,\omega_i) - l_0(k,\omega_i) - \sum_{\nu=1}^{n}\left[l_\nu(k,\omega_i) + l_{-\nu}(k,\omega_i)\right]\right)^2 \tag{5.6}$$

where $\omega_i = i\Delta\omega$, $\Delta\omega = 2\pi/t_0$ is the resolution of the MD-generated spectra, and p is the number of positive frequencies ω_i for which the spectra were calculated. The minimizations with respect to the $3n+2$ parameters A_ν, ω_ν and γ_ν were carried out independently for $S_{NN}(k,\omega)$ and $S_{CC}(k,\omega)$, without making any attempt to correlate *a priori* the two sets of parameters, which are obviously not independent since the collective modes are expected to contribute, albeit with different weights, to both spectra. For each wavenumber k, the minimizations were carried out with one ($n = 0$), three ($n = 1$) and five ($n = 2$) Lorentzians. The improvement of the least-squares fit achieved with a larger number of Lorentzians was considered to be significant only when it led to a decrease of χ^2, overcoming the unfavourable bias factor $(3n+2)$ in the definition (5.6).

It is clear that the representations (5.5) do not apply in the high-frequency limit, since they lead to divergent frequency sum rules [23]. Hence it is not surprising that the Lorentzian fits do not yield accurate wings of the MD data for the spectra $S_{aa}(k,\omega)$; the latter decay much faster than $1/\omega^2$, reflecting the trivial free-particle motion which dominates the high-frequency behaviour, but hardly affects the collective dynamics in which we are interested here.

The results of the above analysis are summarized in the following section, starting with the limiting situation of pure metal ($x = 1$).

6. Concentration dependence of the extended collective modes

The case of the pure metal is the simplest to analyse, because only one correlation function ($S_{NN}(k,\omega) \equiv S_{11}(k,\omega)$) is left. Numerous neutron and numerical experiments have been devoted to collective dynamics in liquid alkali metals [24], but almost exclusively near the melting point; the present data are, to the best of our knowledge, the first MD results for an expanded liquid metal ($T \simeq 10^3$ K). MD simulations were carried out for the experimental molar volume ($V = 61\,\mathrm{cm^3\,mol^{-1}}$) and for a significantly lower molar volume ($V = 50\,\mathrm{cm^3\,mol^{-1}}$), close to that of the pure salt ($x = 0$); no qualitative differences were found between the two sets of data. The density fluctuation spectra are dominated by extremely sharp Brillouin peaks, up to wavenumbers k of the order of $1\,\mathrm{\AA^{-1}}$; an

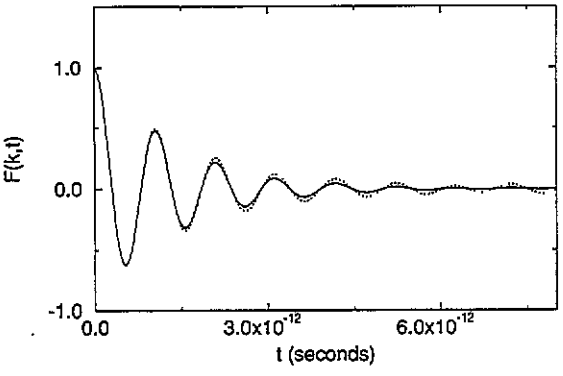

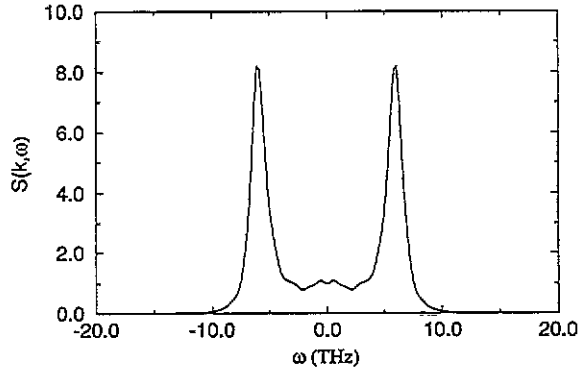

Figure 5. MD results for the normalized density autocorrelation function $F(k, t)$ (upper curve) and its spectrum (dynamical structure factor) $S(k, \omega)$ (lower curve) for pure K, and for a wavenumber $k = 0.318\,\text{Å}^{-1}$. The dotted curve in the upper figure represents the raw MD data, while the full curve represents the smoothed (filtered) data, as explained in the text. Angular frequencies ω are in THz.

example is shown in figure 5. In that range of k values, there is practically no trace of a central Rayleigh peak, as would be expected if the constant-pressure and constant-volume specific heats were very close ($C_P \simeq C_V$), leading to a very small value of the Landau–Placzek ratio $I_R/2I_B = C_P/C_V - 1$ in the hydrodynamic (small-k) limit. It may be concluded that $C_P \simeq C_V$ (i.e. that entropy fluctuations are small) as is indeed the case in simple liquid metals. Not surprisingly, the three-Lorentzian fits lead to χ^2 values which are an order of magnitude smaller than those achieved with a single Lorentzian up to $k \simeq 1\,\text{Å}^{-1}$, and only beyond $k \simeq 1.5\,\text{Å}^{-1}$ does the single-Lorentzian description lead to a comparable accuracy. The dispersion curve $\omega(k)$ is pictured in figure 6, which also shows the Lorentzian width parameter γ_1. The shape of the dispersion curve for the extended sound mode closely resembles that observed in earlier experimental and numerical work on liquid alkali metals [24], going through a well defined maximum, but there is no evidence for a sound propagation gap for wavenumbers in the vicinity of the Brillouin zone boundary ($k \simeq 1.5\,\text{Å}^{-1}$).

The observed spectra $S_{aa}(k, \omega)$ change dramatically when salt is added, even in modest proportions, to the metal. Indeed, the relaxation of concentration fluctuations, linked to the interdiffusion of the two ionic species, lead to a strong central peak in the spectra, i.e. to an enhancement of the Lorentzian $l_0(k, \omega)$ in the representation (5.5). On the metal-rich side, MD simulations were carried out for concentrations $x = 0.9$ and $x = 0.8$, with a qualitatively similar result. $S_{NN}(k, \omega)$ and $S_{CC}(k, \omega)$ have similar shapes, with well separated Brillouin

side peaks up to $k \simeq 0.7\,\text{Å}^{-1}$ for $x = 0.8$, but the relative intensity of the central peak is much larger in $S_{NN}(k, \omega)$ compared to $S_{CC}(k, \omega)$, as illustrated in figure 7, for $k = 0.341$. The confrontation with the pure-metal data at a comparable wavenumber (shown in figure 5), is striking. The dispersion curves, $(\omega_1(k), \gamma_1(k))$ against k, derived from three-Lorentzian fits to $S_{NN}(k, \omega)$ and $S_{CC}(k, \omega)$, are plotted in figure 8. The frequencies $\omega_1(k)$ associated with the two spectra are close, at all wavenumbers, giving much weight to the interpretation that they correspond to the same collective acoustic mode. This mode also shows up quite clearly in the cross-correlation spectrum $S_{NC}(k, \omega)$, pictured in figure 9; notice that the interdiffusion relaxation mode contributes a negative central peak to that spectrum.

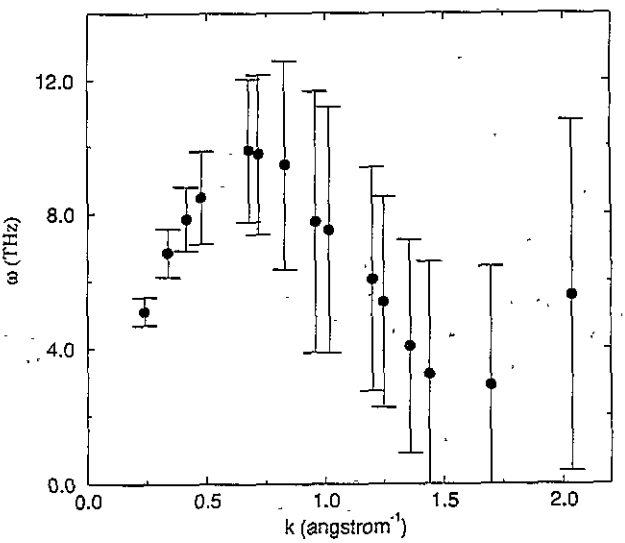

Figure 6. Dispersion curve of the longitudinal mode in the pure metal. The dots correspond to the resonance frequency ω_1 in a three-Lorentzian representation (5.5) of the dynamical structure factor, while the vertical bars represent the width γ_1 of the resonance.

Comparison of figures 6 and 8 shows that the dispersion curves for the extended sound mode are very similar, both qualitatively and quantitatively, for the pure-metal ($x = 1$) and the metal-rich solution ($x = 0.8$). The propagation of sound modes seems to be little affected by the presence of anions in moderate proportions. In particular the sound velocity hardly changes, as may be seen from table 1.

The situation changes more significantly in the range of intermediate concentrations, where we have explored $x = 0.6$, 0.4 and 0.3. Most noteworthy, separate Brillouin side peaks no longer appear in $S_{NN}(k, \omega)$, even at the smallest accessible wavenumbers, but are replaced by distinct shoulders on the high-frequency side of the intense central peak. Examples of $S_{NN}(k, \omega)$ obtained for $x = 0.6$ are shown in figure 10(*a*). $S_{CC}(k, \omega)$, on the other hand, continues to exhibit well defined sharp side peaks at small wavenumbers, as may be seen from figure 10(*b*). A three-Lorentzian analysis of the two sets of spectra yields the dispersion curves shown in figures 11 and 12 for $x = 0.6$ and 0.4. Apart from a stronger damping, a splitting of the dispersion curves associated with number and charge density fluctuations is now clearly apparent. The two dispersion curves cross at $k \simeq 0.7\,\text{Å}^{-1}$, the frequencies $\omega_C(k)$ associated with the charge fluctuations lying well above the corresponding characteristic frequencies $\omega_N(k)$ of density fluctuations for $k \leqslant 0.7\,\text{Å}^{-1}$, the contrary being true above that wavenumber. Guided by the theoretical analysis of [13], we associate $\omega_N(k)$ with the sound mode, whereas $\omega_C(k)$ may be regarded as the characteristic frequency of a

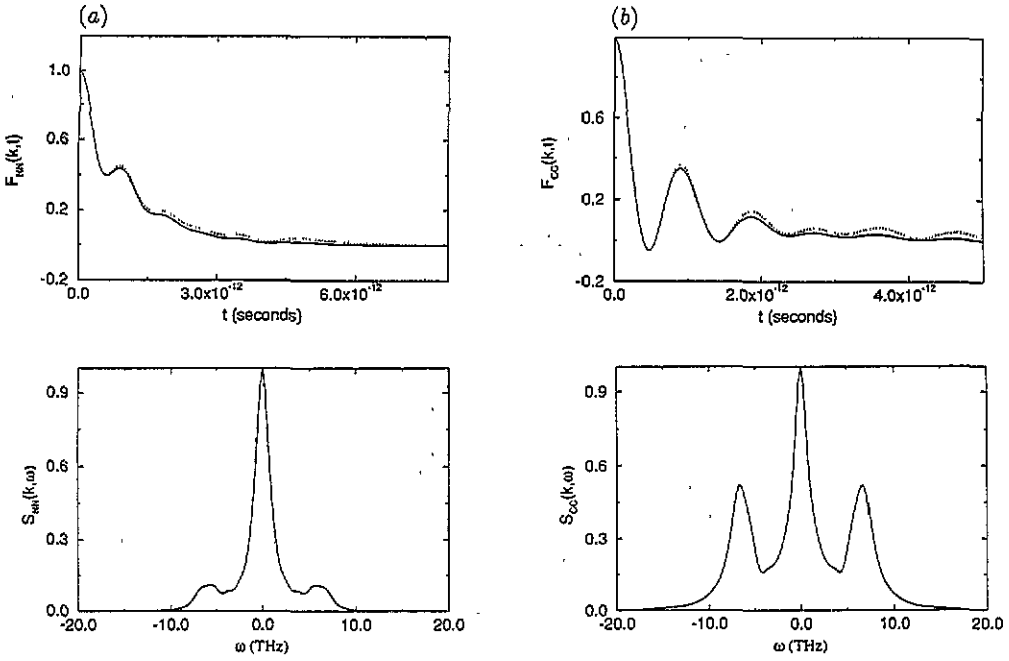

Figure 7. (*a*) Normalized density autocorrelation function $F_{NN}(k,t)$ and associated density fluctuation spectrum $S_{NN}(k,\omega)$ for metal concentration $x = 0.8$ and wavenumber $k = 0.341\,\text{Å}^{-1}$. The dotted and full curves for $F_{NN}(k,t)$ correspond to raw and smoothed MD data. (*b*) Same as figure 7(*a*), but for $F_{CC}(k,t)$ and $S_{CC}(k,\omega)$.

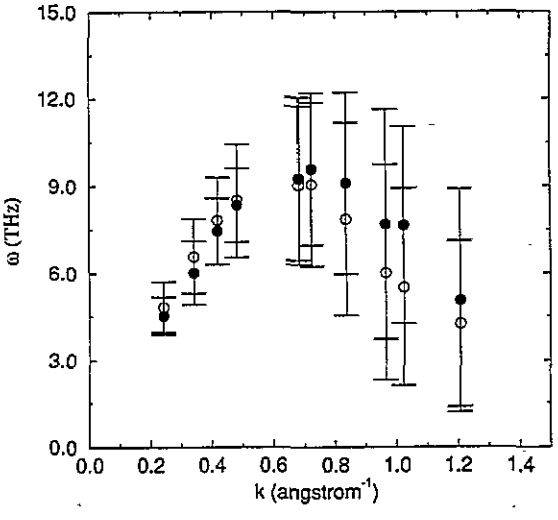

Figure 8. Dispersion curves derived from the density fluctuation spectra $S_{NN}(k,\omega)$ (filled circles) and charge fluctuation spectra $S_{CC}(k,\omega)$ (open circles) for a metal concentration $x = 0.8$.

high-frequency optic mode. We consider the latter to be a remnant of the well known optic (or plasmon) mode observed in molten salts [22], i.e. in the $x = 0$ limit, to which we shall return later.

The existence of two extended longitudinal collective modes should *a priori* imprint a signature on the two spectral functions, although one may expect the sound mode to dominate the density fluctuation spectrum $S_{NN}(k,\omega)$, and the optic mode to dominate the

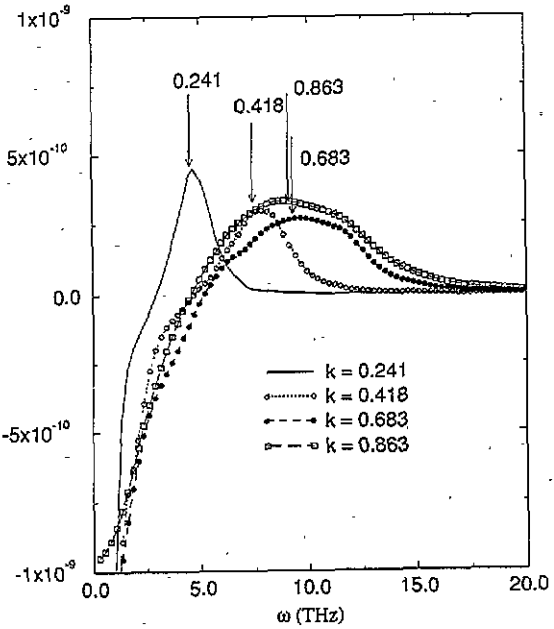

Figure 9. Spectrum $S_{NC}(k, \omega)$ (in seconds) of the density–charge cross-correlation function for a metal concentration $x = 0.8$ and wavenumbers $k = 0.241$ (full curve), $k = 0.418$ (open circles), $k = 0.683$ (filled circles) and $k = 0.863\,\text{Å}^{-1}$ (squares). The arrows indicate the positions of the peaks in the density fluctuation spectrum $S_{NN}(k, \omega)$ at the same wavenumbers.

charge fluctuation spectrum $S_{CC}(k, \omega)$. In an attempt to find evidence for two propagating extended modes in each of the two spectra, we carried out least-squares fits with a five-Lorentzian representation ($n = 2$ in (5.5)). While no significant lowering of χ^2, relative to a three-Lorentzian representation, was found for $S_{NN}(k, \omega)$, the improvement turned out to be sizeable (up to a factor of two) in the case of $S_{CC}(k, \omega)$. However, while the values of the frequency $\omega_1(k)$ changed little in going from a three-Lorentzian to a five-Lorentzian representation, our MD data were not sufficiently accurate to allow any firm conclusions concerning the second frequency $\omega_2(k)$.

In the salt-rich regime ($x = 0.2$ and $x = 0.1$) the collective behaviour becomes more and more ionic like, featuring very pronounced optic side peaks in $S_{CC}(k, \omega)$ at increasingly high frequencies, as illustrated in figure 13(*a*) for $x = 0.1$. Notice, however, that the side peaks vanish both at small wavenumbers ($k \leqslant 0.4\,\text{Å}^{-1}$) and large wavenumbers ($k \geqslant 1.2\,\text{Å}^{-1}$); beyond this upper limit, $S_{CC}(k, \omega)$ narrows dramatically, indicating a considerable slowing down of charge relaxation [22].

The characteristic optic frequency $\omega_C(k)$ at the smallest accessible wavenumber almost doubles in going from $x = 0.2$ to $x = 0.1$, a circumstance which we attribute to the decreasing screening power of the electrons (cf. the values of the effective screening length in table 1). The dispersion curves of the optic and acoustic modes, as determined from three-Lorentzian fits to $S_{CC}(k, \omega)$ and $S_{NN}(k, \omega)$, are shown in figures 14 and 15 for $x = 0.2$ and $x = 0.1$ respectively. The five Lorentzian fits reduce the χ^2 values only slightly, without allowing any new insight, due again to the insufficient statistical quality of the MD data.

The pure-salt ($x = 0$) results are in agreement with expectation: the charge fluctuation spectrum exhibits a pair of very sharp optic ('plasmon') peaks, with nearly k-independent damping, up to $k \simeq 1.2\,\text{Å}^{-1}$, whereafter the spectrum shrinks to an extremely narrow central peak, which gradually broadens beyond $k \simeq 1.6\,\text{Å}^{-1}$. This scenario, partly illustrated in figure 13(*b*), agrees with previous simulations of other alkali halide melts [22, 25]. The plot

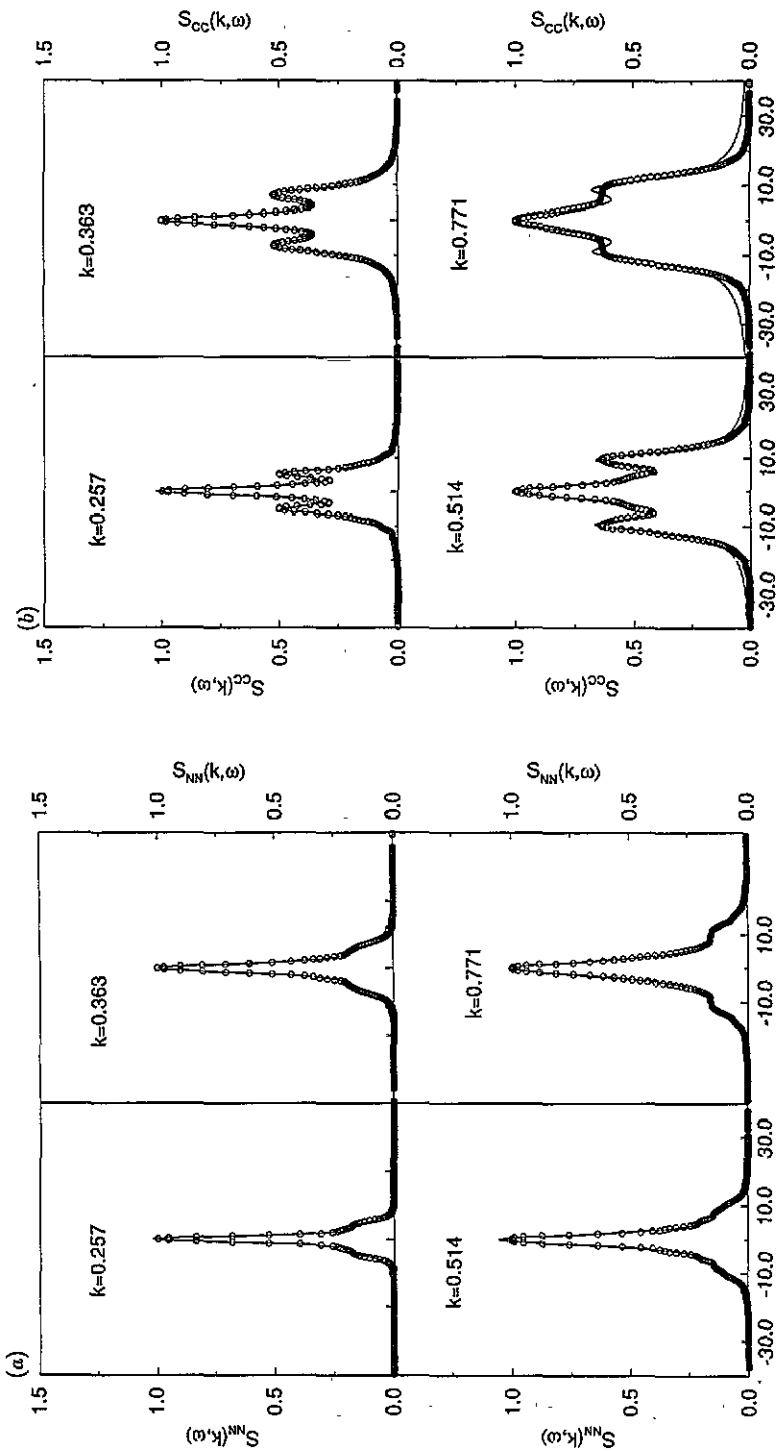

Figure 10. *(a)* Density fluctuation spectra $S_{NN}(k,\omega)$ against angular frequency ω (in THz) for a metal concentration $x = 0.6$, and wavenumbers $k = 0.257$, 0.363, 0.514 and 0.771 Å^{-1}. The open circles are the MD data, while the full curves correspond to the best fit within the three-Lorentzian representation (5.5) ($n = 1$). *(b)* Same as figure 10*(a)*, but for $S_{CC}(k,\omega)$.

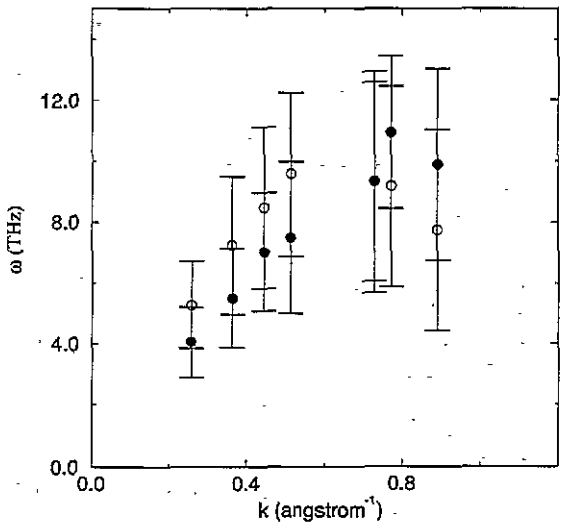

Figure 11. Dispersion curves for $x = 0.6$; symbols as in figure 8.

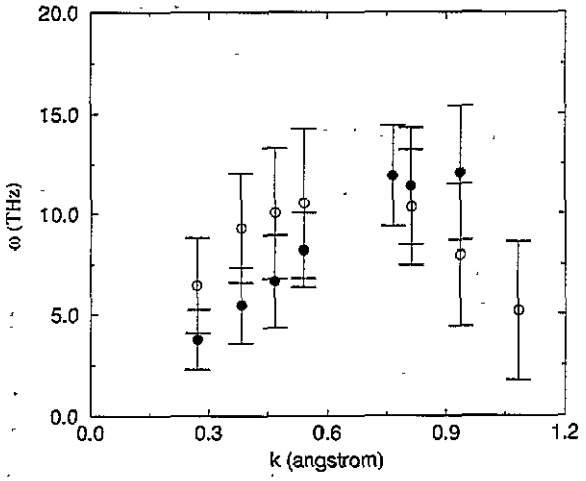

Figure 12. Dispersion curves for $x = 0.4$; symbols as in figure 8.

of $\omega_C(k)$ against k in figure 16 exhibits the usual pronounced negative dispersion, typical of strongly coupled ionic systems. In view of the sharpness of the plasmon peaks, the long-wavelength limit of $\omega_C(k)$ (which is not directly accessible to the MD simulations) may be estimated from the ratio of the fourth- and second-frequency moments of $S_{CC}(k, \omega)$, which is easily calculated, with the result [22, 26]

$$\lim_{k\to 0} \omega_C^2(k) \simeq \lim_{k\to 0} \frac{\overline{\omega^4(k)}}{\overline{\omega^2(k)}} = \tfrac{2}{3}\omega_p^2 + \frac{n}{6M} \int g_{12}(r) \nabla^2 v_{12}^s(r)\, \mathrm{d}\boldsymbol{r} \tag{6.1}$$

where M denotes the reduced mass of an anion–cation pair, $\omega_p = \left(2\pi n e^2/M\right)^{1/2}$ is the plasma frequency and $v_{12}^s(r)$ is the short-range part (i.e. the Born–Mayer repulsion) of the anion–cation pair potential (2.1). Calculating (6.1) with the MD-generated pair distribution function $g_{12}(r)$, one obtains the estimate $\omega_C(k = 0) = 40.7$ THz, which extrapolates nicely the optic branch of the dispersion curves in figure 16 to zero wavenumber.

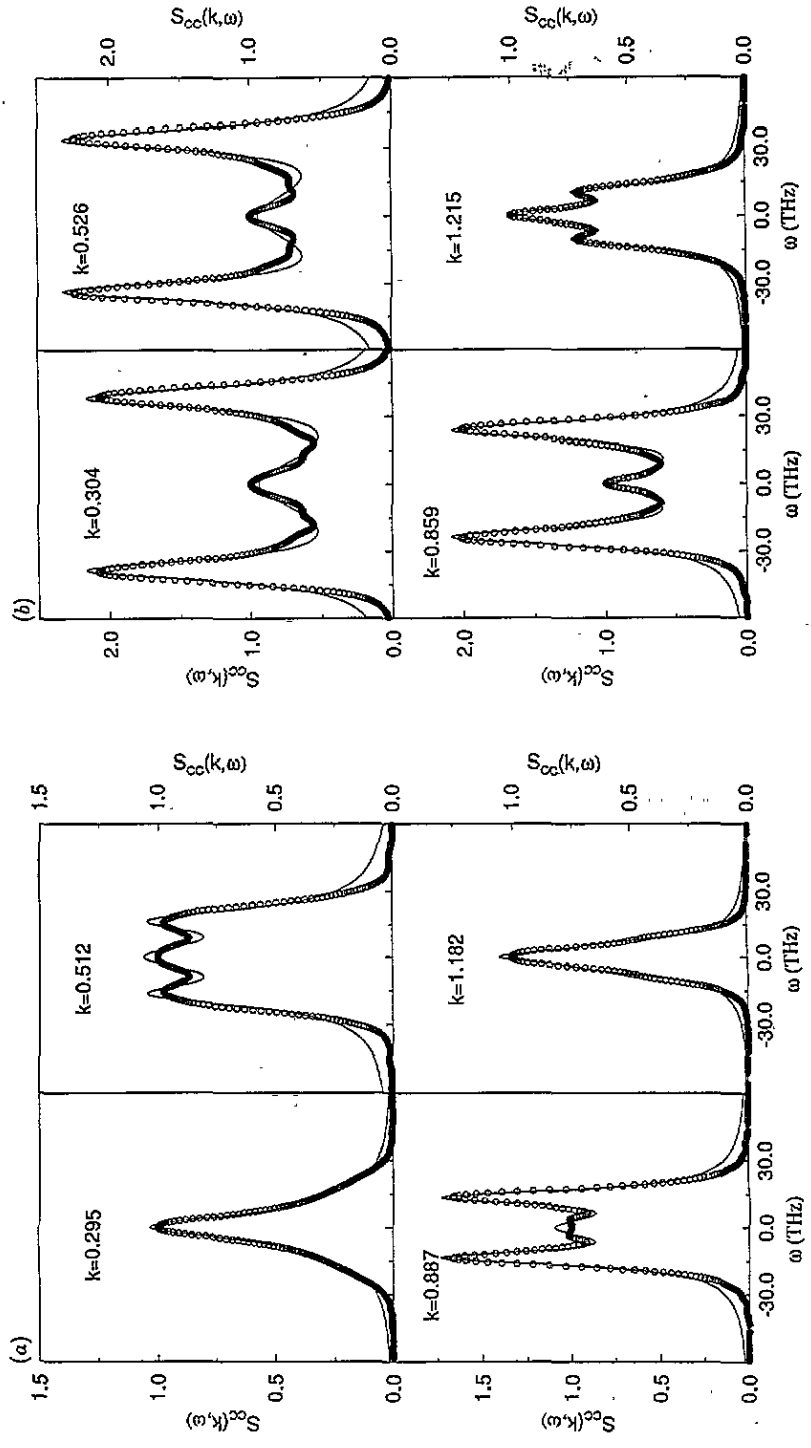

Figure 13. (*a*) Charge fluctuation spectra $S_{CC}(k,\omega)$ for a metal concentration $x = 0.1$, and wavenumbers $k = 0.295$, 0.512, 0.887 and 1.182 Å^{-1}. Symbols as in figure 10(*a*) and (*b*). (*b*) Same as (*a*), but for the pure salt ($x = 0$) and slightly different wavenumbers.

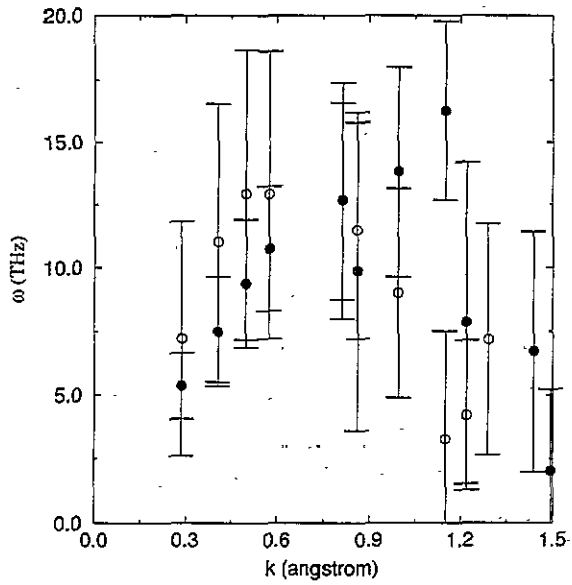

Figure 14. Dispersion curves for metal concentration $x = 0.2$; symbols as in figure 8.

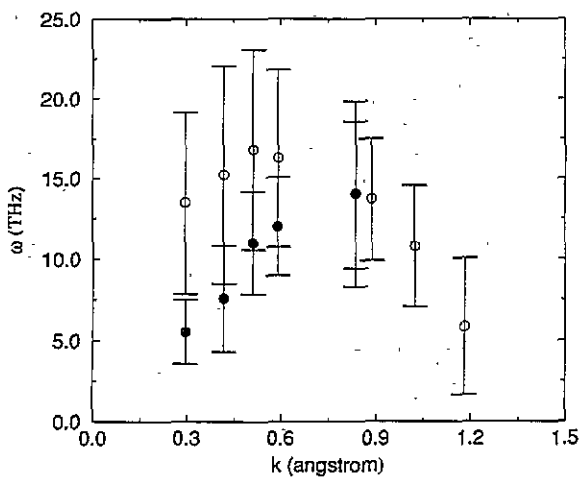

Figure 15. Dispersion curves for metal concentration $x = 0.1$; symbols as in figure 8.

Another check of the consistency of the MD data is provided by the width of the central peak. The five-Lorentzian analysis, which yields the best fit to the low-frequency behaviour of $S_{CC}(k,\omega)$, indicates a nearly constant width up to $k \simeq 0.6\,\text{Å}^{-1}$. Neglecting the k-dependent contribution of entropy fluctuations, the small-k, ω limit of $S_{CC}(k,\omega)$ is given precisely by a Lorentzian of width governed by the DC conductivity σ [12, 27]:

$$\frac{S_{CC}(k,\omega)}{S_{CC}(k)} = \frac{1}{\pi}\frac{4\pi\sigma}{\omega^2 + (4\pi\sigma)^2} \qquad k, \omega \to 0. \tag{6.2}$$

Comparing (6.2) to the observed width, σ is estimated to be 0.8 THz, which compares favourably with the estimate $\sigma \simeq 1.1$ THz based on the Nernst–Einstein relation [22]

$$\sigma \simeq \frac{ne^2}{2k_B T}(D_1 + D_2) \tag{6.3}$$

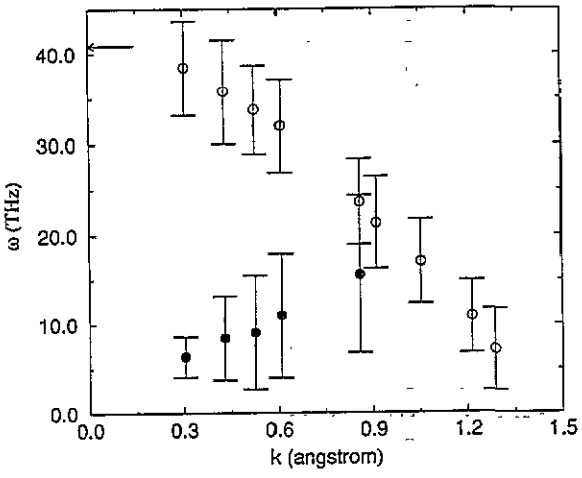

Figure 16. Dispersion curves for metal concentration $x = 0$; symbols as in figure 8. The arrow indicates the value of the frequency $\omega_C(k = 0)$ obtained by the formula (6.1).

where D_1 and D_2 are taken from table 1; negative deviations of about 20% from the approximate relation (6.3) are typical of molten alkali halides [22, 28].

Since mass and charge density fluctuations are practically orthogonal in the present model, the optic mode does not affect $S_{NN}(k, \omega)$. The latter does not exhibit Brillouin side peaks, even at the lowest wavenumber accessible in the present simulations ($k \simeq 0.3\,\text{Å}^{-1}$), but a three-Lorentzian fit points towards heavily damped extended sound modes up to $k \simeq 0.8\,\text{Å}^{-1}$. Sound modes are known to be heavily damped in molten-salt simulations [22], but the present data provide convincing evidence for a propagating acoustic mode over a range of wavenumbers that are easily accessible to MD simulations and inelastic neutron scattering experiments.

Direct evaluation of $S_{NC}(k, \omega)$ for several wavenumbers shows that, as expected, the cross correlations are totally negligible (i.e. remain within the statistical noise level), except at very low frequencies.

7. Discussion

The present set of MD simulations of longitudinal collective modes in a simple model of metal–salt solutions confirms, at least qualitatively, the crossover scenario predicted by the generalized hydrodynamics analysis of [13]. Density fluctuations in the expanded liquid metal are dominated by a surprisingly long-lived acoustic mode, which propagates up to $k \simeq 1.5\,\text{Å}^{-1}$, at which wavenumber the imaginary part of the frequency becomes comparable to its real part. Contrary to the situation in liquids close to the triple point [14, 15], the extended mode analysis shows no evidence of a propagation gap in the vicinity of the Brillouin zone boundary.

The generalized sound dispersion curve and damping hardly change upon adding a small amount of salt (in practice down to $x \simeq 0.8$), and the sound mode is also apparent in the charge fluctuation spectrum, $S_{CC}(k, \omega)$.

However, as x is further lowered into the equimolar range, the extended mode analysis based on the phenomenological representation (5.5) points towards the coexistence of two propagating longitudinal modes: the extended sound mode, which becomes more and more heavily damped as x decreases, while dominating the density fluctuation spectrum; and a

higher-frequency mode, which gradually dominates the charge fluctuation spectrum, which we tentatively identify with the extended optic mode predicted by the theoretical analysis of [13]. The latter is not a hydrodynamic mode, since it cannot be associated with a conserved momentum variable, but rather a remnant of the propagating high-frequency plasmon mode typical of ionic liquids; this mode is pre-eminent in $S_{CC}(k, \omega)$ of the pure salt ($x = 0$), where it gives rise to long-lived resonances with a distinctly negative dispersion. As metal is added, the valence electrons (which are assumed to be completely delocalized in the present model) screen the long-ranged Coulomb interactions between ions, leading to a dramatic lowering of the optic frequency at long wavelengths.

In principle the two propagating longitudinal modes should be visible, although with different weights, in both fluctuation spectra at intermediate concentrations, where number and charge densities are not even approximately orthogonal. For that reason we have attempted least-squares fits to the MD spectra with five Lorentzians (i.e. $n = 2$ in the representation (5.5)). The resulting weighted χ^2 turned out to be invariably larger than that achieved with only three Lorentzians ($n = 1$) in the case of $S_{NN}(k, \omega)$, but significant improvements were observed for the charge fluctuation spectrum $S_{CC}(k, \omega)$ in several cases. However, the data were of insufficient statistical quality to allow any firm conclusions to be drawn concerning the non-dominant propagating mode. We believe that the extended mode analysis may be successfully generalized to situations with more than one propagating mode only if extremely accurate experimental or simulation data are available.

Finally, some comments concerning the validity of the simple model, embodied in the potentials (2.1), are in order. As already stated earlier the model should be regarded as the simplest possible interpolation between the pure-metal and pure-salt limits, for which it retains the essential physical features. The simple linear Thomas–Fermi description of electron screening at intermediate densities is certainly too crude to allow quantitatively reliable predictions for future experiments, although it may have qualitative validity. An obvious drawback of the above linear screening model is that it does not account for the obvious asymmetry in the short-range screening of anions and cations by the valence electrons. The latter attract, while the former repels the electrons, and the corresponding difference in the local polarization is not properly accounted for by the long-wavelength form of the electron dielectric function $\epsilon_0(k)$. Another defect of the model is that it neglects ionic polarization.

In order to overcome the shortcomings of the model investigated in this paper (for which the MD simulations yield, in principle, 'exact' results), we are presently exploring an *ab initio* approach, combining MD for the ions and density functional theory for the valence electrons, in view of a more realistic description of metal–salt solutions. Since long phase-space trajectories are required in a study of collective dynamics, the original Car–Parrinello method [29], based on the Kohn–Sham formulation of density functional theory, is not at present applicable. An alternative scheme, based on improved Thomas–Fermi–von Weiszacker density functionals, is presently being developed [30].

Acknowledgments

The authors are grateful to Josette Dupuy, Jean-François Jal and Laurent Hily for their constant interest in this work and for making available the unpublished experimental results shown in figure 2, and to Neil Ashcroft and Paul Madden for stimulating comments. AM gratefully acknowledges financial support of the European Community under Science contract SC1*0153-C(EDB).

References

[1] Bredig M A 1964 *Molten Salt Chemistry* ed. M Blander (New York: Wiley-Interscience)
[2] Jal J F, Mathieu C, Chieux P and Dupuy J 1990 *Phil. Mag.* **62** 351
Chieux P, Jal J F, Hily L, Leclercq F and Damay P 1991 *J. Physique* **4** C5–3
Dupuy J, Hily L, Jal J F, Chieux P and Gaspard J R 1991 *J. Physique* **4** C5–31
[3] Garbade K and Freyland W 1988 *Z. Phys. Chem.* **156** 169
[4] Chabrier G, Senatore G and Tosi M P 1982 *Nuovo Cim.* D **1** 409
[5] Chabrier G and Hansen J P 1983 *Mol. Phys.* **50** 901
[6] Chabrier G and Hansen J P 1986 *Mol. Phys.* **59** 1345 (1986)
[7] Ashcroft N W and Stroud D 1978 *Solid State Physics* **33** ed. F Seitz and D Turnbull (New York: Academic)
[8] Mathieu C, Jal J F, Dupuy J, Suck J B and Chieux P 1990 *Nuovo Cim.* D **12** 673
[9] Chabrier G, Hansen J P and Joanny J F 1986 *J. Phys. C: Solid State Phys.* **19** 4443
[10] Postogna F and Tosi M P 1980 *Nuovo Cim.* **55** 399
[11] Chabrier G and Joanny J F 1987 *J. Phys. C: Solid State Phys.* **20** 3787
[12] Giaquinta P V, Parrinello M and Tosi M P 1976 *Phys. Chem. Liq.* **5** 305
[13] Hansen J P and Yoshida F 1991 *J. Phys. Cond. Matt.* **3** 2583
[14] de Schepper I M and Cohen E G D 1980 *Phys. Rev.* A **22** 287; 1982 *J. Stat. Phys.* **27** 223
[15] de Graaf L A 1989 *Static and Dynamic Properties of Liquids* ed. M Davidovic and A K Soper (Berlin: Springer)
van Well A A, Verkerk P, deGraaf L A, Suck J B and Copley J R D 1985 *Phys. Rev.* A **31** 3391
[16] Tosi M P and Fumi F G 1964 *J. Phys. Chem. Solids* **25** 31
[17] Ichimaru S 1982 *Rev. Mod. Phys.* **54** 1017
[18] Parrinello M and Rahman A 1984 *J. Chem. Phys.* **80** 860
[19] Fois E, Selloni A and Parrinello M 1989 *Phys. Rev.* B **39** 4812
[20] Lantelme F and Turq P 1982 *J. Chem. Phys.* **77** 3177
[21] Baus M 1977 *Physica* **88A** 319, 336, 591
[22] Hansen J P and McDonald I R 1985 *Phys. Rev.* A **11** 2111
[23] Hansen J P and McDonald I R 1986 *Theory of Simple Liquids* 2nd edn (New York: Academic)
[24] Kambayashi S and Kahl G 1992 *Europhys. Lett.* **18** 421
[25] Copley J R D and Rahman A 1976 *Phys. Rev.* A **13** 2276
Adams E M, McDonald I R and Singer K 1977 *Proc. R. Soc.* A **357**.37
Dixon M 1983 *Phil. Mag.* B **47** 509, 531; **48** 13
[26] Abramo M C, Parrinello M and Tosi M P 1973 *J. Non-Metals* **2** 67
[27] Vieillefosse P 1977 *J. Physique Lett.* **38** 443
[28] Ciccotti G, Jacucci G and McDonald I R 1976 *Phys. Rev.* A **13** 426
[29] Car R and Parrinello M 1985 *Phys. Rev. Lett.* **55** 2471
Remler D K and Madden P A 1990 *Mol. Phys.* **70** 921
[30] Meroni A, Hansen J P and Madden P A 1993 to be published